Nano Research

Open Access

Research Article

A hierarchical NiFeOOH@CeO_{2-x} nanosheets array boosts electrocatalytic activity and durability at high current densities for water oxidation

Wei Zhang, Liyang Xiao, Xiaorui Huang, Chunyan Han, Ying Liu, Jingtong Zhang, Haiwen Tan, Rui Zhang, Pengfei Yin, Cunku Dong, Hui Liu, Xiwen Du, and Jing Yang ✉

Institute of New Energy Materials, Key Laboratory of Advanced Ceramics and Machining Technology of Ministry of Education, School of Materials Science and Engineering, Tianjin University, Tianjin 300072, China

Cite this article: *Nano Research*, **2025**, *18*, 94907213. https://doi.org/10.26599/NR.2025.94907213

ABSTRACT: The oxygen evolution reaction (OER) reaction kinetics of nickel-iron (oxy)hydroxides (NiFeOOH) is limited by their weak adsorption of OER intermediates. Herein, a hierarchical NiFeOOH@CeO_{2-x} nanosheets array was *in situ* grown on a nickel foam by a facile laser direct writing method, which exhibits superior OER activity and durability at high current densities in alkaline electrolytes. The hierarchical nanosheets array exposes abundant catalytic active sites, which greatly promote OER reaction rate. The strong electronic interaction at the NiFeOOH/CeO_{2-x} interface leads to favorable electron transfer from $Ni^{2+/3+}$ and Fe^{3+} to $Ce^{3+/4+}$. The Ni sites with high valences show enhanced OH^- adsorption and also promote the formation of *OOH intermediate, thereby greatly improving OER intrinsic activity. The oxygen deficient CeO_{2-x} primary sheets guarantee good electrical conductivity. Such a well-designed catalytic electrode requires overpotentials of only 229 and 287 mV to achieve current densities of 50 and 500 mA·cm^{-2}, respectively, and sustains superior stability at 500 mA·cm^{-2} and 1 A·cm^{-2}.

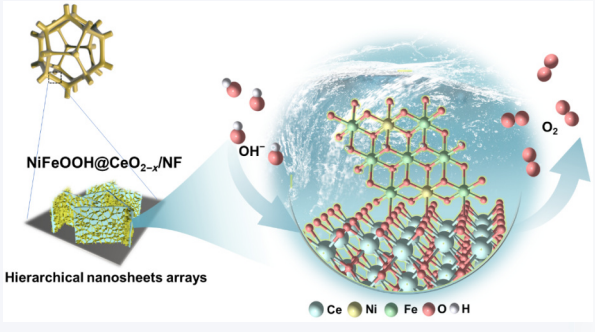

KEYWORDS: hierarchical nanosheets, transition metal (oxy)hydroxides, oxygen evolution reaction, laser direct writing, water splitting

1 Introduction

The oxygen and hydrogen evolution reactions (OER/HER) play key roles in green hydrogen production via electrochemical water splitting [1–3]. Complicated four proton-coupled electron transfer process in OER causes its sluggish kinetics [4–6]. To overcome the bottleneck, it is urgent to manufacture electrocatalysts with fast electron/proton transfer capability and high intrinsic activity for large-scale applications [7]. Noble metal ruthenium- and iridium-based oxides (RuO_2, IrO_2) are regarded as superior electrocatalysts, but their commercial applications are limited by insufficient reserves, high cost, and poor OER durability [8, 9]. Currently, various non-noble transition-metal-based catalysts (e.g. oxides [10], sulfides [11], nitrides [12], phosphides [13], and (oxy)hydroxides [14, 15]) have exhibited excellent OER electrocatalytic performance and considered as promising candidates for OER catalysis.

Nickel-iron-based (oxy)hydroxides (NiFeOOH) have been regarded as prominent catalysts for OER due to their relatively high catalytic activity, abundant resources, low cost, and environmental friendliness [16, 17]. However, NiFeOOH catalysts still suffer from unsatisfactory adsorption/desorption strength for OER intermediates [18], poor electrical conductivity [19], and inferior stability [17] during electrocatalytic water splitting. To dates, several strategies have been employed to further improve the OER activity of NiFeOOH, such as doping with N, S, B, Mo, etc. [20], introducing multi-dimensional defects (e.g., phase boundaries, atomic defects, etc.) [18], and designing heterostructures [21]. As we know, it has been widely accepted that the OER active sites of NiFeOOH are mainly located at the edge of two-dimensional sheet, but not on the basil plane [22]. Therefore, optimizing the electronic structures of edge active sites and meantime maximizing the amount of optimized active sites would substantially enhance the OER activity.

Hierarchical structures, especially hierarchical nanosheets, have

Received: September 20, 2024; **Revised:** November 27, 2024
Accepted: December 24, 2024

✉Address correspondence to yang_jing@tju.edu.cn

been demonstrated to expose abundant active sites on the surface and edge of secondary nanosheets as well as a large number of active sites at the interface between primary and secondary sheets [23, 24]. Besides, favorable electron transfer at the interface would optimize the electronic structure of active sites to enhance their intrinsic activity [25]. However, it is still challenging to effectively improve the OER activity of NiFeOOH-based catalysts at high current densities by rationally design and facial preparation of hierarchical nanosheets structures.

It has been reported that high-valence transition metal active sites could overcome the limitations of linear scaling relationships, accelerate reaction kinetics, and provide high intrinsic activity for OER [26]. However, according to the Hund's rule, the formation and stabilization of high-valence metal sites are thermodynamically unfavorable [1, 27]. Therefore, elevating valence states of Ni and/or Fe ions in NiFeOOH to achieve superior OER activity has become quite challenging. Cerium dioxide (CeO_2), a rare-earth metal oxide, has widely attracted attention due to its flexible conversion between Ce^{3+} and Ce^{4+} states [28, 29]. The multivalence property of CeO_2 offers an opportunity to realize strong electronic interactions with other transition-metal compounds [30]. Hence, CeO_2 might be a good choice to optimize the valence states of metal active sites in NiFeOOH via hetero-interface electron interaction for fast OER kinetics. To date, there have been reported studies on either CeO_2 nanoparticles grown on NiFe LDH nanosheets or nanosheets composed of NiFeOOH and CeO_2 phases [31–34]. It is well known that NiFe LDH transforms into NiFeOOH during the OER process, and the real OER active sites are actually located on the edge of NiFeOOH nanosheets. However, the exploration to fundamentally boost the intrinsic activity of the edge active sites were still insufficient, moreover, the number of edge active sites of the NiFeOOH nanosheets were also limited. Therefore, it is still challenging to enhance both the OER intrinsic activity and number of edge active sites of NiFeOOH.

Herein, we prepared hierarchical NiFeOOH@CeO_{2-x} nanosheets arrays *in situ* grown on nickel foam (NF) via electro-deposition and millisecond laser direct writing (MLDW) method. The secondary NiFeOOH nanosheets have dimensions of approximately 35 nm in width and 3 nm in thickness. Such dense ultra-fine NiFeOOH nanosheet arrays expose abundant edge active sites, thus improving catalytic reaction rates at high current densities. Meantime, partial electrons transfer from Ni and Fe in the secondary NiFeOOH nanosheets to Ce in the primary CeO_2 microsheets at the heterogeneous interface. The resulted high valence Ni sites are more likely to enhance OH^- adsorption and facilitate *OOH formation, thereby boosting OER intrinsic activity. The presence of oxygen vacancies in the primary CeO_2 microsheets also expedites electron transport throughout the whole electrode. The NiFeOOH@CeO_{2-x}/NF electrode needs overpotentials of only 229 and 287 mV to achieve current densities of 50 and 500 mA·cm^{-2} in 1.0 M KOH, respectively, and maintain excellent durability at 1000 mA·cm^{-2} up to 500 h. An alkaline water electrolyzer with NiFeOOH@CeO_{2-x}/NF as the anode and PtNi/NF as the cathode only requires record-low cell potentials of 1.42 and 1.60 V to achieve current densities of 10 and 500 mA·cm^{-2} for overall water splitting, indicating high potential for practical water electrolysis.

2 Experimental

2.1 Chemical reagents

All chemicals were purchased without any further purification. Nickel foams (NF, thickness 1.5 mm) were purchased from Tianjin Aiweixin Chemical Technology Co., Ltd. Potassium hydroxide (KOH, GR, 85%) was obtained from Aladdin Industrial Corporation. Cerium(III) nitrate nonahydrate ($Ce(NO_3)_3·9H_2O$, 99.5%) was produced by Shanghai Meryl Chemical Technology Co., LTD. Nickel(II) sulfate hexahydrate ($NiSO_4·6H_2O$, GR, 99%) and iron(II) sulfate heptahydrate ($FeSO_4·7H_2O$, 99%) were selected from Kemat (Tianjin) Chemical Technology Co., Ltd. Iron(II) chloride hexahydrate ($FeCl_2·6H_2O$, 99.7%) was bought from Tianjin Fengchuan Chemical Reagent Technology Co., LTD. Platinum carbon (Pt/C, 20%), Nafion solution (5%) were purchased from Shanghai Macklin Biochemical Co., Ltd. Ruthenium oxide (RuO_2) was produced by Tianjin Incole Union Technology Co., Ltd. Deionized water (DIW) was obtained from Tianjin Keruisi Co., Ltd. with resistance greater than 18 MΩ.

2.2 Synthesis of CeO_2/NF electrode

CeO_2/NF was synthesized using an electro-deposition method. Prior to synthesis, a piece of NF (2 cm × 3 cm) was sequentially cleaned with 3.0 M dilute hydrochloric acid, ethanol, and deionized water for 15 min via ultrasonication treatment. In a standard three-electrode electrochemical cell, NF, graphite rod, and saturated calomel electrode (SCE) were utilized as the working electrode, counter electrode, and reference electrode, respectively. $Ce(NO_3)_3·9H_2O$ (2.5 mmol) was dissolved in deionized water (50 mL) by stirring for 5 min. Subsequently, electro-deposition was carried out under a constant potential of −1.2 V for 500 s. The as-prepared sample was washed three times with deionized water and then dried in 60 °C vacuum oven for 30 min.

2.3 Synthesis of NiFeOOH@CeO_{2-x}/NF electrode

The NiFeOOH@CeO_{2-x}/NF electrode was prepared by performing the MLDW treatment on CeO_2/NF in a mixed solution of Ni salt and Fe salt by using a millisecond-pulsed Nd:YAG laser. The electrode was progressively moved by an *XY* motorized translation stage, thereby achieving a self-supporting electrode with a predefined laser treated area.

2.4 Synthesis of NiFeOOH@CeO_2/NF electrode

The NiFeOOH@CeO_2/NF electrode was obtained by annealing NiFeOOH@CeO_{2-x}/NF at 300 °C for 4 h in oxygen atmosphere.

2.5 Synthesis of NiFeOOH/NF electrode

The NiFeOOH/NF electrode was fabricated via the MLDW method. Specifically, laser irradiation was conducted directly on NF immersed in a Fe salt solution.

2.6 Preparation of RuO_2/NF and Pt/C/NF electrodes

5 mg of RuO_2 powder (or 5 mg of Pt/C powder) was added in 970 μL of water, followed by the addition of Nafion solution (5 wt.%, 30 μL). The mixture was sonicated for 30 min to obtain a well-dispersed catalyst ink. 100 μL of ink was dropped onto the NF and then dried in a vacuum oven at 60 °C for 5 h.

2.7 Characterizations

Crystal structures of all the samples were characterized by using X-ray diffraction (XRD, Bruker, D8 advance). Morphologies were measured on scanning electron microscopy (SEM, JEOL, S-4800). The thickness of the sample was determined by atomic force microscopy (AFM, Brooker, Dimension icon). Transmission

electron microscopy (TEM), scanning transmission electron microscopy (STEM), selected area electron diffraction (SAED), high-resolution TEM (HR-TEM), energy-dispersive spectroscopy (EDS) and EDS mapping were performed on JEM-F200 transmission microscope (JEOL, Japan). X-ray photoelectron spectroscopy (XPS) measurements were recorded on Kratos Axis Supra scanning microprobe spectrometer. Electron paramagnetic resonance (EPR) tests were undertaken on the German Bruker A300-10/12 model. The contents of chemical elements were determined by using inductively coupled plasma-mass spectrometry (ICP-MS) on an Agilent 5110. Raman and *in-situ* Raman tests were performed using 532 nm laser of the French Horiba model. Nitrogen isotherms were obtained at 77 K on an automatic specific surface and aperture distribution analyzer.

2.8 Electrochemical measurements

Electrochemical measurements of electrodes were carried out on an electrochemical analyzer (CHI 660E, Shanghai, China) within a standard three-electrode system at room temperature. The as-prepared electrodes with a geometric area of 0.25 cm^2 were directly used as the working electrodes. A graphite rod and Hg/HgO electrode were used as counter and reference electrode, respectively. Freshly prepared aqueous solutions of 1.0 M KOH were used as the electrolyte. Cyclic voltammograms (CV) and linear sweep voltammetry (LSV) curves were obtained using a scan rate of 5 and 50 $mV{\cdot}s^{-1}$, respectively. All polarization curves were corrected for 85% *iR* compensation. The potentials were calculated with respect to the reversible hydrogen electrode (RHE) based on the Nernst equation: $E(\mathrm{RHE}) = E(\mathrm{SCE}) + 0.059\mathrm{pH} + 0.098$ V. Electrochemical impedance spectroscopy (EIS) tests were acquired in a frequency range from 0.1 Hz to 100 kHz at the overpotential of 0.45 V vs. the RHE. The electrochemical double-layer capacitance (C_{dl}) was determined using CV curves at 40, 80, 120, 160 and 200 $mV{\cdot}s^{-1}$ from 0.068 to 0.118 V vs. RHE. By plotting the difference in current density within non-Faradaic potential range against the scan rates, the C_{dl} values were derived from the linear slopes and utilized to represent the corresponding electrochemically active surface area (ECSA). The ECSA can be calculated based on Eq. (1)

$$\mathrm{ECSA} = C_{dl}/C_s \quad (1)$$

The specific capacitance C_s refers to the capacitance per unit area of a flat surface, with a value of 40 $\mu F{\cdot}cm^{-1}$ being utilized. The long-term durability was tested using amperometric *i–t* curve mode at 500 $mA{\cdot}cm^{-1}$ for 280 h.

The Mott–Schottky (M–S) experiment was conducted in 0.5 M Na_2SO_4 solution at a frequency of 1 kHz using a three-electrode system. The counter electrode comprised a platinum electrode, the reference electrode utilized an Ag/AgCl electrode, and the working electrode featured the synthesized catalytic electrode. The electrical conductivity between the catalysts and NF substrates was measured using the four-probe test method. The M–S equation (Eq. (2)) is presented as follows

$$1/c^2 = 2/\varepsilon\varepsilon_0 A^2 e N_d (V - V_{fb} - k_B/T) \quad (2)$$

where N_d is the donor concentration, k_B is the Boltzmann constant, T is the absolute temperature, ε_0 is the vacuum permittivity, ε is the relative permittivity (dielectric constant), A is the electrode area, e is the elementary charge, V is the applied voltage, and V_{fb} is the flat band potential. The methods used to calculate the turnover frequency (TOF) are described in the supporting information.

To demonstrate the application of catalyst for overall water splitting, a two-electrode electrolysis cell was assembled, utilizing the NiFeOOH@CeO_{2-x}/NF electrode as the anode and a PtNi/NF (reported in our previous work [35]) as the cathode. The LSV curve was recorded at a scan rate of 5 $mV{\cdot}s^{-1}$ with 85% *iR* compensation. The stability test was conducted in 1.0 M KOH electrolyte at a constant current density of 500 $mA{\cdot}cm^{-2}$. Furthermore, a single-cell water electrolyzer was also built to compare the performance of different electrodes under industrial conditions (80 °C, 6.0 M KOH).

3 Results and discussion

3.1 Synthesis and characterization of NiFeOOH@CeO_{2-x}/NF

The synthetic route of the hierarchical nanosheets arrays is demonstrated in Fig. 1. Particularly, CeO_2 primary sheets were firstly *in situ* grown on NF using an electro-deposition method, followed by the growth of NiFeOOH secondary nanosheets on the surface of CeO_2 sheets by using the MLDW method. The shape and size of laser processing area could be precisely controlled via a programmable *XY* mechanical translation stage, indicating its potential in scalable synthesis.

The SEM image of CeO_2/NF (Fig. S1 in the Electronic Supplementary Material (ESM)) shows a uniform microsheets array grown on NF with a sheet size of ~ 1.5 μm. The X-ray diffraction (XRD) pattern of CeO_2/NF (Fig. 2(a)) displays diffraction peaks at 28.5°, 33.0°, 47.4°, and 51.8°, which accord with cubic CeO_2 (JCPDS: 78-0694). The XRD pattern of NiFeOOH@CeO_{2-x} only shows diffraction peaks of CeO_2 and NF. The absence of XRD peaks of NiFeOOH could be due to ultra-thin and small size and/or poor crystallinity of the NiFeOOH secondary nanosheets. The SEM images (Fig. 2(b) and Fig. S2 in the ESM) confirm the presence of ultra-small nanosheets with an average dimension of 35 nm grown on the surface of CeO_2 microsheet, which form a hierarchical sheets-on-sheets structure. The AFM image (Fig. 2(c)) indicates that the thickness of the ultra-thin secondary nanosheets is about 3 nm. Raman spectroscopy (Fig. 2(d)) was employed to confirm the existence of both NiFeOOH and CeO_2 for the as-prepared hierarchical nanosheets arrays. The characteristic peaks observed at 200, 315 and 680 cm^{-1} are attributed to the characteristic vibration peaks of Fe–O of NiFeOOH, whereas the peaks at 480 and 555 cm^{-1} correspond to Ni–O for NiFeOOH [36, 37]. The Raman peak of CeO_2 at 465 cm^{-1} overlaps with that of Ni–O at 480 cm^{-1} for the hierarchical nanosheets arrays. To further confirm the crystal structures of the primary microsheets and secondary nanosheets, TEM analysis was performed. As shown in Fig. 2(e), the TEM image indicates that the primary sheets (size of ~ 1.5 μm) and secondary nanosheets (size of ~ 35 nm) form a hierarchical structure, which is consistent with the SEM image (Fig. 2(b)). The corresponding selected area electron diffraction (SAED) pattern display diffraction rings corresponding to (111), (200), (222), (331), and (422) crystal planes of CeO_2, as well as (200), (151), and (022) lattice planes of γ-FeOOH. As shown in Fig. 2(f), the high-resolution TEM (HR-TEM) image reveals good crystalline structure. The lattice plane spacing of 3.10 Å is consistent with (111) crystal planes of CeO_2, respectively, and the spacing of 1.93 Å

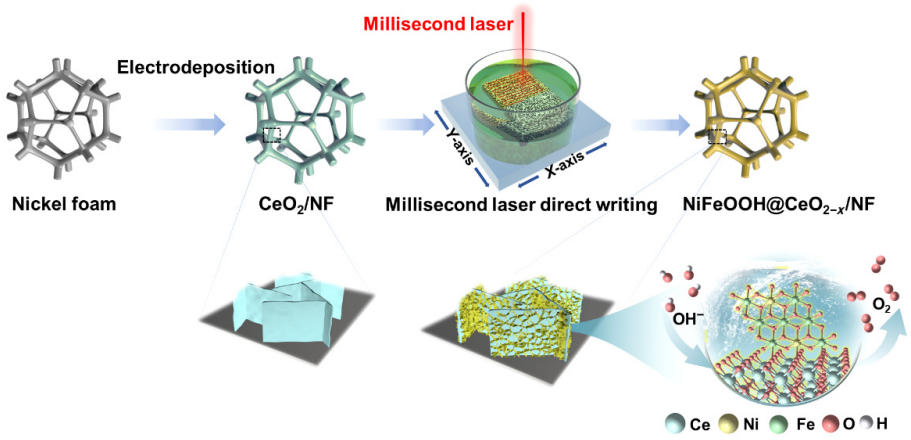

Figure 1 The synthetic route of hierarchical NiFeOOH@CeO_{2-x} nanosheets arrays.

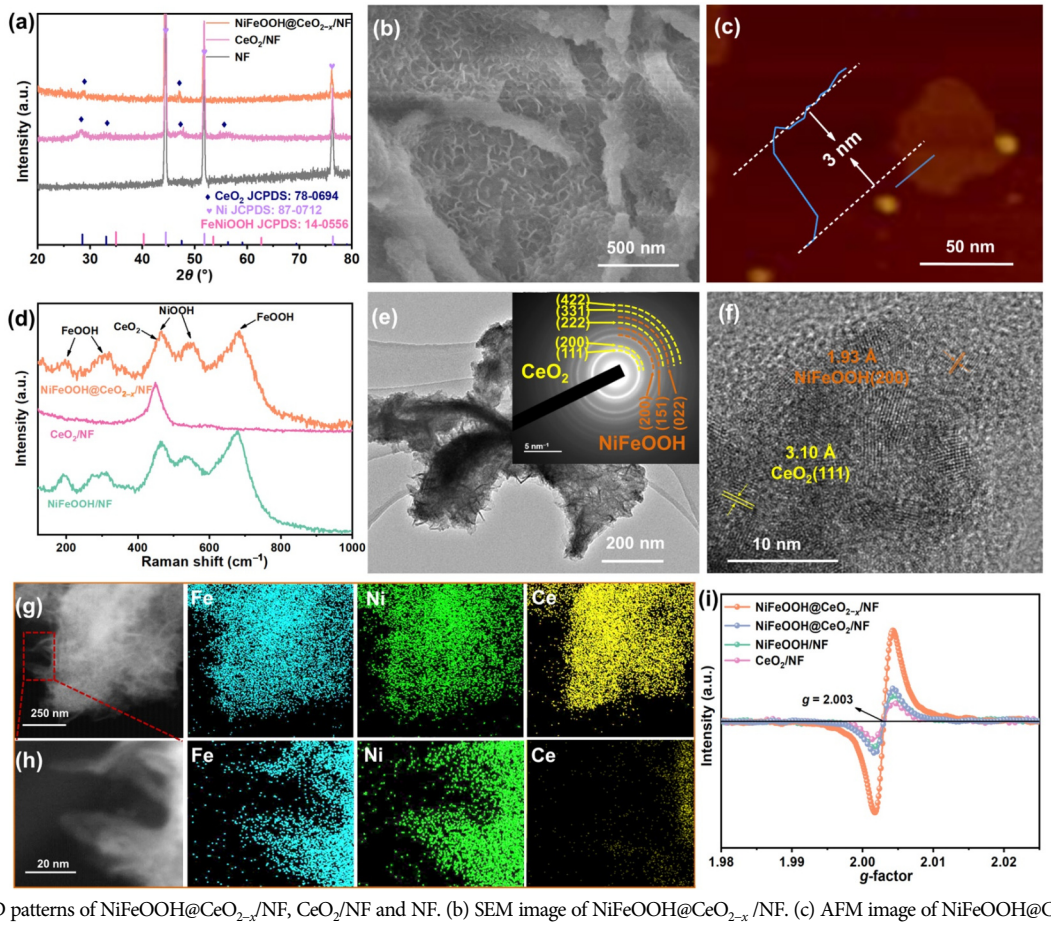

Figure 2 (a) XRD patterns of NiFeOOH@CeO_{2-x}/NF, CeO_2/NF and NF. (b) SEM image of NiFeOOH@CeO_{2-x} /NF. (c) AFM image of NiFeOOH@CeO_{2-x}/NF and the corresponding height profile. (d) Raman spectra of NiFeOOH@CeO_{2-x} /NF, CeO_2/NF and NiFeOOH/NF. (e) TEM image of NiFeOOH@CeO_{2-x}, the inset is SAED pattern of partial region. (f) HR-TEM image of NiFeOOH@CeO_{2-x}. (g) STEM image and EDS elemental mapping images of Ni, Fe, and Ce for NiFeOOH@CeO_{2-x}. (h) STEM image and EDS elemental mapping images of Ni, Fe, and Ce for NiFeOOH. (i) EPR spectra of NiFeOOH@CeO_{2-x} /NF, NiFeOOH@CeO_2/NF, NiFeOOH/NF, and CeO_2/NF.

corresponds to (200) crystal plane of γ-FeOOH. According to the high-angle annular dark-field scanning transmission electron microscopy (HAADF-STEM) image and the corresponding elemental mapping by EDS (Fig. 2(g)), the hierarchical sheet contains Ni, Fe, and Ce elements. Elemental mapping images of the secondary NiFeOOH nanosheets (Fig. 2(h)) confirm that Fe and Ni with an atomic ratio of 2.8:1 are uniformly distributed over the nanosheets without any doping Ce elements. ICP-MS measurements were also performed to determine the Ni, Fe, and Ce contents for NiFeOOH@CeO_{2-x}. As shown in Table S1 in the ESM, the ratio of Fe and Ni is approximately 2.6:1, which is consistent with the EDS-mapping results. All of the above characterizations confirm the successful preparation of hierarchical NiFeOOH@CeO_2/NF nanosheets array.

Our previous studies showed that the MLDW method would easily introduce crystal structure defects into the as-prepared

samples, such as edge dislocations in alloy nanocatalysts [35, 38], oxygen vacancies in spinel oxides [39], etc. In this work, EPR spectroscopy was also recorded to examine the presence of any defects in NiFeOOH@CeO_2/NF. As depicted in Fig. 2(i), a strong symmetric EPR signal (*g*-value of 2.003) was observed for NiFeOOH@CeO_2/NF, which could be attributed to trapped unpaired electrons within the oxygen vacancies [40]. This suggests that the MLDW treatment could introduce abundant oxygen vacancies into the hierarchical nanosheets arrays.

To further determine whether the oxygen vacancies are in NiFeOOH and/or CeO_2 for NiFeOOH@CeO_2/NF, and also explore the impact of hieratical structure on the electronic structure of catalysts, two control samples (NiFeOOH@CeO_2/NF and NiFeOOH/NF) were prepared, and all these samples were subsequently subjected to X-ray photoelectron spectroscopy (XPS) measurements. NiFeOOH@CeO_2/NF was obtained by annealing NiFeOOH@CeO_{2-x}/NF at 300 °C for 4 h in oxygen atmosphere to eliminate the oxygen vacancies. NiFeOOH/NF was prepared using the MLDW method (see Experimental section in the ESM for preparation details). The characterization results of control samples are presented in Figs. S3–S7 in the ESM. The hierarchical NiFeOOH@CeO_2 nanosheets array owns the same phase composition and chemical element content as NiFeOOH@CeO_{2-x}. NiFeOOH/NF also exhibit uniform nanosheets structure in which the nanosheets are 250 nm in width and the atomic ratio of Fe and Ni is same as NiFeOOH@CeO_{2-x}/NF (2.8:1). As shown in Fig. 2(i), the EPR signals suggest that the annealing process indeed reduced the oxygen vacancy content a lot for NiFeOOH@CeO_2/NF, and the NiFeOOH/NF prepared by MLDW method has much lower oxygen vacancy content than NiFeOOH@CeO_{2-x}/NF. To some extent, this implies that oxygen vacancies might primarily exist in CeO_2 but not in NiFeOOH for NiFeOOH@CeO_{2-x}/NF. More evidence would be demonstrated in the following XPS analysis.

As seen in Fig. 3(a), NiFeOOH@CeO_{2-x}/NF (with rich oxygen vacancies) and NiFeOOH@CeO_2/NF (with poor oxygen vacancies) both show Ni $2p_{1/2}$ and $2p_{3/2}$ XPS peaks at 855.2 and 872.4 eV attributed to Ni^{2+}, peaks at 856.4 and 874.0 eV attributed to Ni^{3+} [41], and satellite peaks at 861.9 eV. Compared to NiFeOOH/NF, the $Ni^{2+/3+}$ peaks for hierarchical NiFeOOH@CeO_{2-x}/NF and NiFeOOH@CeO_2/NF shift to higher binding energies by 0.3 eV, suggesting that the electron densities of $Ni^{2+/3+}$ sites are reduced owning to the formation of interface between NiFeOOH and CeO_{2-x} (or CeO_2) for NiFeOOH@CeO_{2-x}/NF and NiFeOOH@CeO_2/NF. As shown in Fig. 3(b), NiFeOOH@CeO_{2-x}/NF and NiFeOOH@CeO_2/NF both exhibit Fe 2p XPS peaks at 711.5 and 725.2 assigned to Fe^{3+} [42] and two satellite peaks at 719.3 and 733.2 eV. Compared to NiFeOOH/NF, the Fe^{3+} peaks for NiFeOOH@CeO_{2-x}/NF and NiFeOOH@CeO_2/NF also shift to higher binding energies by 0.3 eV, indicating that the electron densities of Fe^{3+} sites are also reduced due to the formation of interface between NiFeOOH and CeO_{2-x} (or CeO_2). Meanwhile, as seen in Fig. 3(c), NiFeOOH@CeO_{2-x}/NF and NiFeOOH@CeO_2/NF both show Ce 3d XPS peaks at 882.5, 888.8, 898.5, 901.0, 907.0, and 916.7 eV which are associated with Ce^{4+}, and peaks at 885.1 and 903.5 eV attributed to Ce^{3+} [43, 44]. In comparison with CeO_2/NF, the $Ce^{3+/4+}$ peaks for NiFeOOH@CeO_{2-x}/NF and NiFeOOH@CeO_2/NF shift to lower binding energy regions by 0.4 eV, implying that the electron densities of $Ce^{3+/4+}$ sites increase due to the formation of

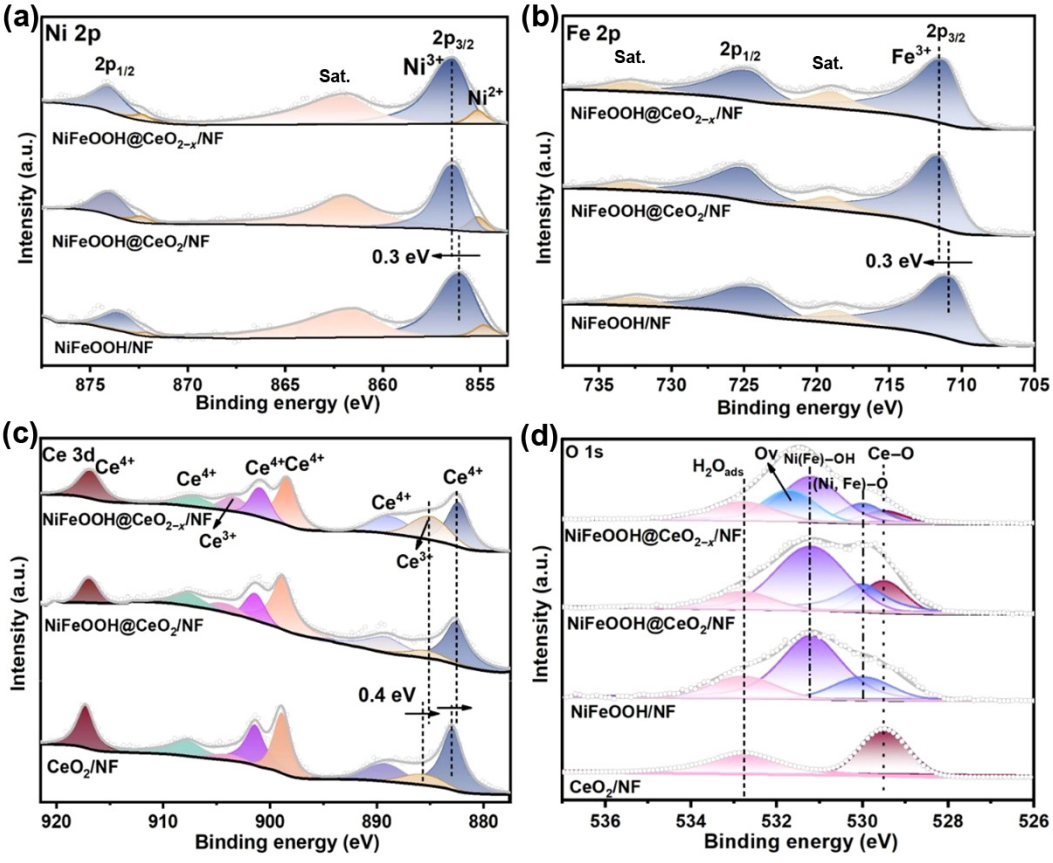

Figure 3 Ni 2p (a) and Fe 2p (b) XPS spectra of NiFeOOH@CeO_{2-x}/NF, NiFeOOH@CeO_2/NF and NiFeOOH/NF. Ce 3d (c) and O 1s (d) XPS spectra of NiFeOOH@CeO_{2-x}/NF, NiFeOOH@CeO_2/NF, NiFeOOH/NF and CeO_2/NF.

interface between NiFeOOH and CeO_{2-x} (or CeO_2). Based on the above analysis, it can be inferred that there is a strong electronic interaction between secondary NiFeOOH nanosheets and primary CeO_{2-x} (or CeO_2) sheets at the heterogeneous interface of NiFeOOH@CeO_{2-x}/NF and NiFeOOH@CeO_2/NF, where electrons partially transfer from $Ni^{2+/3+}$ and Fe^{3+} sites to $Ce^{3+/4+}$ sites.

Moreover, by calculating the peak area, the ratio of Ce^{4+}/Ce^{3+} for NiFeOOH@CeO_{2-x}/NF and NiFeOOH@CeO_2/NF are determined as 3.71:1 and 6.45:1, respectively, which suggest an average valence state of Ce to be 3.78 and 3.86 for NiFeOOH@CeO_{2-x}/NF and NiFeOOH@CeO_2/NF, respectively. Accordingly, the oxygen deficiency in CeO_2 were calculated to be 0.11 and 0.06 for NiFeOOH@CeO_{2-x}/NF and NiFeOOH@CeO_2/NF, respectively. In contrast, the calculated oxygen deficiencies based on $Ni^{3+/2+}$ peak area ratio are 0.05, 0.06, and 0.07 for NiFeOOH@CeO_{2-x}/NF, NiFeOOH@CeO_2/NF, and NiFeOOH/NF, respectively. Specific data are listed in Table S2 in the ESM. These results further confirm that the abundant oxygen vacancies mainly exist in the primary CeO_{2-x} sheets for NiFeOOH@CeO_{2-x}/NF. Besides, as displayed in the O 1 s spectra (Fig. 3(d)), the peaks at 529.5, 530.0, 531.2, 531.8, and 532.8 eV are associated with Ce–O bonds [45, 46], (Ni, Fe)–O bonds, Ni(Fe)–OH bonds [16], oxygen vacancies [30], and surface-adsorbed water molecules, respectively. The presence of peak for oxygen vacancy in NiFeOOH@CeO_{2-x}/NF also suggest a high content of oxygen vacancies [47].

Based on our previous studies, we speculate that millisecond pulsed laser focused on CeO_2/NF causes a strong thermal effect which also heat the surrounding solution to a high temperature in a very short time. The Ni and Fe ions in the saline solution react with surrounding H_2O molecules and dissolved oxygen near the surface of laser-heated CeO_2, leading to rapid nucleation and growth of ultra-fine NiFeOOH nanosheets. Due to the quenching effect of pulse laser irradiation, oxygen defects are not generated in NiFeOOH with high surface energy, but formed in CeO_2 with flexible $Ce^{3+/4+}$ oxidation states.

3.2 OER electrocatalytic activity and durability

The OER electrochemical performance of NiFeOOH@CeO_{2-x}/NF, NiFeOOH@CeO_2/NF, NiFeOOH/NF, and CeO_2/NF electrodes were investigated in 1.0 M KOH solution. All potentials with 85% *iR* correction were referenced vs. the reversible hydrogen electrode (RHE). As shown in Figs. 4(a) and 4(b), NiFeOOH/NF requires overpotentials of 280 and 408 mV to attain 50 and 500 mA·cm^{-2}, respectively. CeO_2/NF exhibits a higher overpotential of 431 mV to reach 50 mA·cm^{-2}. Notably, the hierarchical NiFeOOH@CeO_2/NF electrode requires much lower overpotentials of 246 and 344 mV to achieve current densities of 50 and 500 mA·cm^{-2}, respectively, indicating that the formation of hierarchical nanosheets arrays could enhance the OER activity of NiFeOOH. The hierarchical NiFeOOH@CeO_{2-x}/NF electrode with abundant oxygen vacancies exhibits even lower overpotentials of only 229 and 287 mV at 50 and 500 mA·cm^{-2}, respectively, suggesting that the abundant oxygen vacancies in the primary CeO_{2-x} sheet could further enhance OER activity. NiFeOOH@CeO_{2-x} exhibit outstanding activity compared to the reported non-noble metal catalysts for alkaline OER catalysis (Table S3 in the ESM). As seen in the Tafel

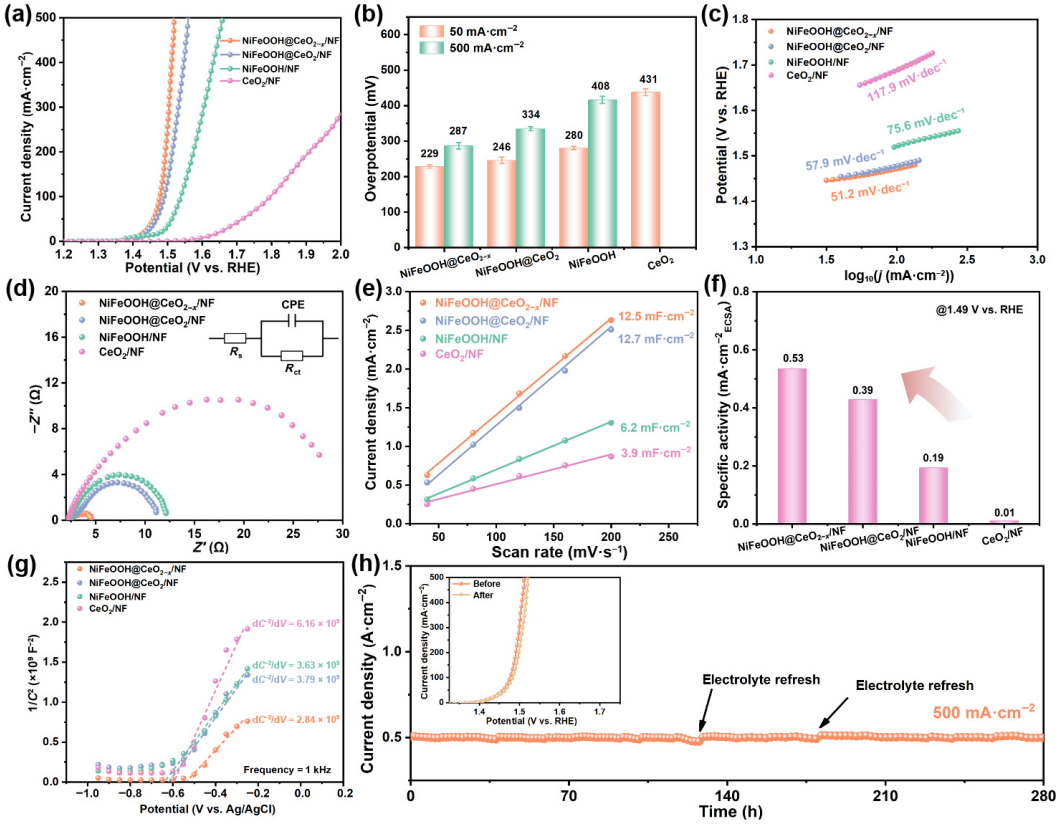

Figure 4 (a) OER LSV curves with 85% *iR*-compensation of NiFeOOH@CeO_{2-x}/NF, NiFeOOH@CeO_2/NF, NiFeOOH/NF, and CeO_2/NF. (b) Comparison of the overpotentials at 50 and 500 mA·cm^{-2}. (c) Tafel plots. (d) EIS Nyquist plots. (e) Capacitive current plotted as a function of different scan rates. (f) Specific activities at the potential of 1.49 V vs. RHE with ECSA correction. (g) The M–S plots. (h) *i*–*t* curve of NiFeOOH@CeO_{2-x}/NF at 500 mA·cm^{-2} for 280 h. (inset: LSV curves of NiFeOOH@CeO_{2-x}/NF before and after 280 h of continuous electrolysis).

plots (Fig. 4(c)), hierarchical NiFeOOH@CeO_{2-x}/NF shows the lowest Tafel slope (51.2 mV·dec^{-1}) compared to NiFeOOH@CeO_2/NF (57.9 mV·dec^{-1}), NiFeOOH/NF (75.6 mV·dec^{-1}), and CeO_2/NF (117.9 mV·dec^{-1}). These result imply that the formation of hierarchical nanosheets arrays and the presence of plentiful oxygen vacancies in CeO_{2-x} accelerate OER kinetics. The charge transfer resistance (R_{ct}) of different catalysts were calculated based on electrochemical impedance spectroscopy (EIS). As illustrated in Fig. 4(d) and Table S4 in the ESM, the formation of hierarchical structure for NiFeOOH@CeO_{2-x}/NF and NiFeOOH@CeO_2/NF results in smaller Nyquist semicircle diameter and thus lower R_{ct} values. And the presence of oxygen vacancies in CeO_{2-x} could further reduce the R_{ct} value. Therefore, the formation of inferface of hierarchical NiFeOOH@CeO_{2-x}/NF and oxygen vacancies in CeO_{2-x} both play important roles in accelerating electron transfer kinetics at catalyst-electrolyte interface.

The specific surface area was measured by recording N_2 sorption isotherms (Fig. S8 in the ESM). The Brunauer–Emmett–Teller (BET) surface areas of NiFeOOH@CeO_{2-x}/NF and NiFeOOH@CeO_2/NF were determined to be 355 and 348 cm^3·g^{-1}, respectively, much higher than NiFeOOH/NF (107 cm^3·g^{-1}) and CeO_2/NF (82 cm^3·g^{-1}). Electrochemical double-layer capacitance (C_{dl}) was also determined by recording CV plots at different scan rates in the non-Faradaic region (Fig. S9 in the ESM). As shown in Fig. 3(e), the C_{dl} values of NiFeOOH@CeO_{2-x}/NF, NiFeOOH@CeO_2/NF, NiFeOOH/NF and CeO_2/NF are calculated to 12.5, 12.7, 6.2, and 3.9 mF·cm^{-2}, respectively. Both the BET surface areas and C_{dl} values confirm that the hierarchical nanosheets array has larger specific surface area. Subsequently, the C_{dl} values were used to estimate the ECSA [48]. As shown in Table S5 in the ESM, NiFeOOH@CeO_{2-x}/NF and NiFeOOH@CeO_2/NF exhibit much higher ECSA values compared to NiFeOOH/NF and CeO_2/NF. The OER current was also normalized to ECSA (Fig. S10 in the ESM) to investigate the specific activity (SA) which is a quantitative measure of intrinsic activity [39]. As shown in Fig. 3(f), NiFeOOH@CeO_{2-x}/NF exhibits the highest SA compared to control samples. In addition, turnover frequency (TOF) of different catalysts were also calculated to reflect the OER intrinsic activity. As shown in Fig. S11 in the ESM, the TOF of NiFeOOH@CeO_{2-x}/NF is 0.49 s^{-1} at 1.49 V, much higher than that of NiFeOOH@CeO_2/NF (0.32 s^{-1}), NiFeOOH/NF (0.15 s^{-1}), and CeO_2/NF (0.01 s^{-1}). These results confirm that NiFeOOH@CeO_{2-x}/NF exhibit higher OER intrinsic activity compared to the control samples, which could be ascribed to the electronic interaction at the interface and the accelerated electron transport due to oxygen vacancies in CeO_{2-x}. M–S plots were made to study the effect of oxygen vacancies in CeO_{2-x} on electron transport of the electrode. As shown in Fig. 4(g), corresponding dC^{-2}/dV values were calculated based on the M–S equation [49]. Since the charge carrier density is inversely related to dC^{-2}/dV, NiFeOOH@CeO_{2-x}/NF has higher charge carrier density and thus higher electrical conductivity than NiFeOOH@CeO_2/NF. As verified in Fig. 3, oxygen vacancies of NiFeOOH@CeO_{2-x} /NF are present in CeO_2 rather than in NiFeOOH. The CeO_2 primary sheet serves as a bridge between NiFeOOH secondary nanosheets and NF substrate. Therefore, the electrical conductivity of CeO_2 would greatly affect the electron transfer and thus OER kinetics. As evidenced by the M–S measurements, the presence of oxygen vacancies in CeO_2 primary sheets enhance the charge carrier density and thus electrical conductivity of NiFeOOH@CeO_{2-x}/NF. This is primarily owning to the enhanced conductivity of CeO_{2-x} with oxygen vacancies which promotes electron transport from NiFeOOH to NF via CeO_{2-x}. Hence, the OER kinetic is further promoted by the presence of oxygen vacancies in CeO_{2-x} primary sheets, as evidence by the Tafel plots (Fig. 4(c)).

Long-term catalytic stability at high current densities is also of great importance for industrial water splitting applications. The stability of NiFeOOH@CeO_{2-x}/NF at 500 mA·cm^{-2} was tested by using a chronoamperometric measurement. As shown in Fig. 4(h), NiFeOOH@CeO_{2-x}/NF was able to maintain the current density for 280 h with only 3.7% decay. LSV curves before and after 280 h of continuous electrolysis differ by only 6 mV at 500 mA·cm^{-2} (inset of Fig. 4(h)). As shown in Fig. S12 in the ESM, even at a current density as high as 1000 mA·cm^{-2}, the NiFeOOH@CeO_{2-x}/NF electrode was also stable up to 500 h, indicating excellent OER durability under the ultra-high current density. The morphology, phase structure, and element valence of NiFeOOH@CeO_{2-x}/NF hardly change after the long-term OER process (Figs. S13–S15 in the ESM). The EPR signals before and after OER stability test are almost identical (Figs. S16 in the ESM), suggesting that the oxygen vacancies are stable during OER. Therefore, the NiFeOOH@CeO_{2-x}/NF electrode show a high potential for applications in industrial water splitting.

3.3 Mechanism for OER performance enhancement

Density functional theory (DFT) calculation was performed to ascertain the catalytic active sites of NiFeOOH@CeO_{2-x}. The atomic structure model of NiFeOOH@CeO_{2-x} was constructed based on the experimental results (HR-TEM and ICP) to study the adsorption of OH^- on Fe, Ni, and Ce sites at the interface of NiFeOOH@CeO_{2-x}. Figures S17(a)–S17(c) in the ESM show the optimized models for OH^- adsorption on Fe, Ni, and Ce sites at the interface, respectively, in which Fe and Ni are both on the edge of NiFeOOH. The calculated Gibbs free energies of OH^- adsorption (Fig. S17(d)) indicate that the Ni site has the strongest adsorption of OH^- compared to Fe and Ce sites, suggesting that Ni is the active site for OER.

To explore the underlying reasons for the high intrinsic activity of hierarchical NiFeOOH@CeO_{2-x} nanosheets arrays in OER process, we also employed sensitive electrochemical techniques for investigation. Firstly, the OER current densities at 1.49 V vs. RHE with the variation of KOH concentrations were plotted for NiFeOOH@CeO_{2-x}/NF, NiFeOOH@CeO_2/NF, and NiFeOOH/NF, in order to explore the adsorption of OH^-. As seen in Fig. 5(a), as KOH concentration increases from 0.1 to 1.5 M, the current density of NiFeOOH/NF gradually increases. When KOH concentration exceeds 1.5 M, the current density hardly changes anymore, indicating that the adsorption of OH^- on NiFeOOH/NF is saturated [50, 51]. In contrast, the current density of NiFeOOH@CeO_{2-x}/NF and NiFeOOH@CeO_2/NF remain almost constant when KOH concentration exceed 1.2 M, indicating that the adsorption of OH^- reaches saturation at lower KOH concentrations. Furthermore, by plotting the slope of $\log_{10}(j)$ against $\log_{10}(C_{KOH})$, the reaction order can be determined (the inset of Fig. 5(a)). The reaction order for NiFeOOH@CeO_{2-x}/NF (1.40) and NiFeOOH@CeO_2/NF (1.43) are much lower than NiFeOOH/NF (1.65), implying that the variation of OH^- concentration has a weaker impact on the OER kinetic for NiFeOOH@CeO_{2-x}/NF and NiFeOOH@CeO_2/NF than NiFeOOH/NF. The above results suggest that NiFeOOH@$Ce0_{2-x}$/NF and NiFe0OH@CeO_2/NF have stronger OH^- adsorption ability than NiFeOOH/NF, probably due to the interfacial Ni active

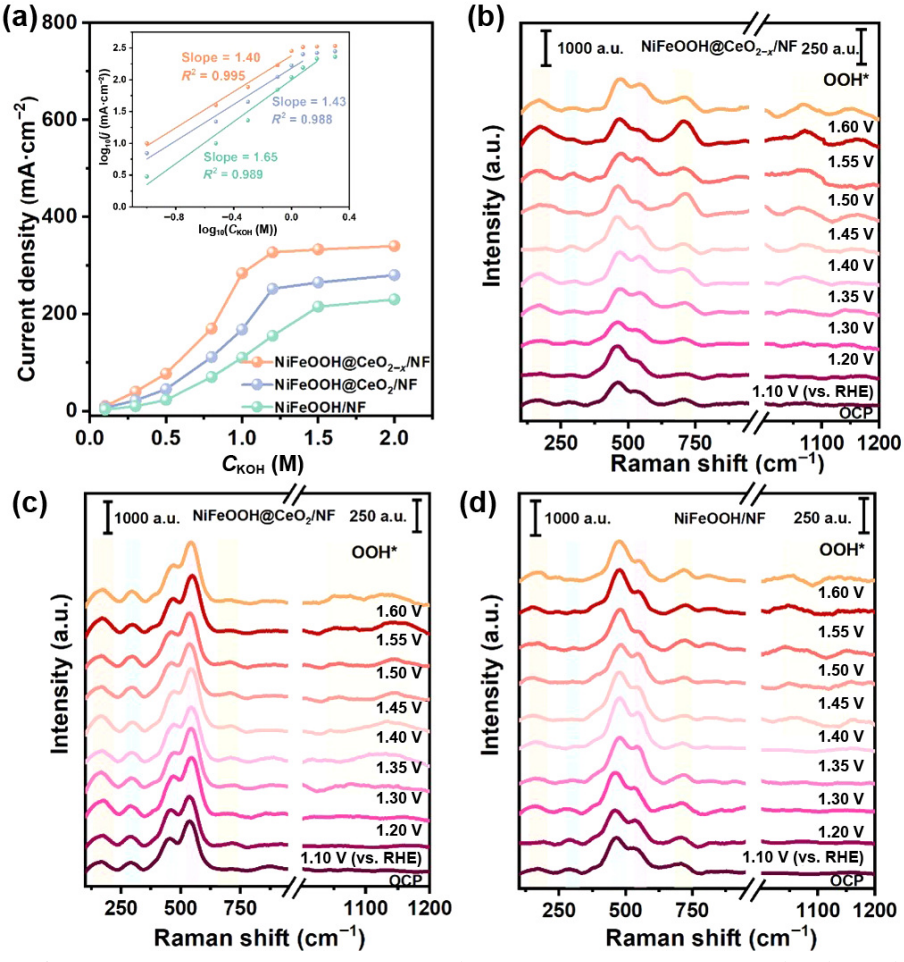

Figure 5 (a) Current density of NiFeOOH@CeO_{2-x}/NF, NiFeOOH@CeO_2/NF and NiFeOOH/NF at 1.49 V vs. RHE in electrolytes with different concentrations of KOH. The inset is the dependence of the j_{KOH} in different concentrations of KOH. *In situ* Raman patterns of (b) NiFeOOH@CeO_{2-x}/NF, (c) NiFeOOH@CeO_2/NF and (d) NiFeOOH/NF at potential from 1.1 to 1.6 V.

sites in higher oxidation states induced by electron transfer between NiFeOOH and CeO_{2-x} (or CeO_2).

To elucidate the dynamics of oxygen-containing intermediates adsorbed on the catalysts surface during the OER process, operando Raman spectroscopy was employed to perform electrochemical assessments on different catalytic electrodes in 1.0 M KOH electrolyte. Within the potential range of 1.1 to 1.6 V vs. RHE, including the open circuit potential (OCP), *in-situ* Raman spectra were collected at the electrode surface (Figs. 5(b)–5(d). In the low wavenumber range, the peaks at 200, 315 and 680 cm^{-1} are characteristic vibrational peaks of Fe–O in NiFeOOH, whereas the principal peaks near 480 and 555 cm^{-1} correspond to Ni–O of NiFeOOH. The Raman peaks at 480 and 555 cm^{-1} correspond to the bending vibration of E_g mode and stretching vibration of A_{1g} mode of Ni–O, respectively [52–54]. According to the literature study [55], the peak intensity ratio between E_g-mode and A_{1g}-mode ($I_{E_g}/I_{A_{1g}}$) is regarded as a descriptor associated with the degree of disorder of NiOOH. The higher $I_{E_g}/I_{A_{1g}}$ values for NiFeOOH@CeO_{2-x}/NF (Fig. 5(b)) and NiFeOOH/NF (Fig. 5(d)) than that for NiFeOOH@CeO_2/NF (Fig. 5(c)) suggest that NiFeOOH@CeO_{2-x}/NF and NiFeOOH/NF are in more disorder γ-NiFeOOH phase, while the annealed sample NiFeOOH@CeO_2/NF is in less disorder β-NiFeOOH phase. This is consistent with the fact that the high-temperature annealing process would transform γ-NiFeOOH to more ordered β-NiFeOOH [56]. In the high wavenumber region, OER intermediates adsorbed on the catalysts surface were detected. Upon increasing the applied potential, a broad band in the range of 1050–1200 cm^{-1} begins to emerge for NiFeOOH@CeO_{2-x}/NF at 1.3 V vs. RHE, which is considered to be the formation of "active oxygen" (OO^-) [39]. By comparing the initial potentials where the OO^- band appears for different catalytic electrodes, the relative energy barriers for OOH* formation can be qualitatively assessed. The hierarchical NiFeOOH@CeO_{2-x}/NF and NiFeOOH@CeO_2/NF nanosheets arrays exhibit identical potential of 1.30 V vs. RHE, at which the OO^- band of OOH* starts to emerge. The initial appearance potential of OO^- band for NiFeOOH/NF is 1.40 V vs. RHE, higher than hierarchical NiFeOOH@CeO_{2-x}/NF and NiFeOOH@CeO_2/NF, suggesting that the formation of hierarchical nanosheets arrays could reduce the energy barrier of OOH* formation. Additionally, the above results also indicate that the presence of oxygen vacancies in the primary CeO_{2-x} sheets of NiFeOOH@CeO_{2-x}/NF could not affect the energy barrier of OOH* formation. Based on the above analysis, we reveal that the formation of hierarchical nanosheets array enhance the OH^- adsorption and promote OOH* formation for OER, probably due to the interfacial electron transfer from $Ni^{2+/3+}$ to $Ce^{3+/4+}$ which induces more highly active Ni ions with high valence. The oxygen vacancies in the primary CeO_{2-x} sheet accelerate electron transport

throughout the whole electrode. Thereby, they both greatly promote the OER kinetics of NiFeOOH@CeO_{2-x}/NF.

3.4 Performance evaluation in overall water splitting

Benefiting from superior catalytic activity of NiFeOOH@CeO_{2-x}/NF electrode for alkaline OER, an alkaline water electrolyzer for overall water splitting was further evaluated. Based on our previous work [35], PtNi alloy rich in edge dislocations was synthesized on NF (denoted as PtNi/NF) using the MLDW method to serve as the cathode for HER. As shown in Fig. 6(a), LSV curves with 85% *iR* correction reveal that PtNi/NF requires lower overpotentials than Pt/C/NF. Subsequently, a dual-electrode water electrolyzer was assembled with NiFeOOH@CeO_{2-x}/NF as the anode and PtNi/NF as the cathode in 1.0 M KOH. As displayed in Fig. 6(b), PtNi/NF||NiFeOOH@CeO_{2-x}/NF couple exhibits excellent water-splitting activity with a low cell voltage of 1.42 and 1.60 V at 10 and 500 mA·cm^{-2}, respectively, which overwhelmingly surpass commercial Pt/C/NF||RuO_2/NF couple. Compared to the theoretical values for HER and OER tests (Fig. 6(c)), the voltage values in electrolyzer tests are close to the theoretical values, indicating that the catalytic electrodes have excellent overall water-splitting performance. The chronoamperometric response of PtNi/NF||NiFeOOH@CeO_{2-x}/NF couple at high current density of 500 mA·cm^{-2} was measured, and negligible activity decay can be observed over 280 h (Fig. 6(d)). The optical photograph taken during the experiment (inset of Fig. 6(d)) indicate that the electrolyzer can operate stably with a fast gas release rate. Besides, a single-cell water electrolyzer was set up to compare the performance of overall water splitting for different electrodes, the optical photograph of which is shown in Fig. S18(a) in the ESM. The PtNi/NF||NiFeOOH@CeO_{2-x}/NF couple exhibits electrolysis voltages of 1.79 and 2.00 V at 400 and 1000 mA·cm^{-2}, respectively, which are lower than that of Pt/C/NF||RuO_2/NF (1.94, 2.28 V), as shown in Fig. 6(e) and Fig. S18(b) in the ESM. The excellent electrocatalytic activity and durability of PtNi/NF||NiFeOOH@CeO_{2-x}/NF demonstrates its potential for practical water electrolysis.

4 Conclusions

In summary, the hierarchical NiFeOOH@CeO_{2-x} nanosheet arrays *in situ* grown on NF were successfully fabricated via electrodeposition and MLDW method. The formation of ultra-fine NiFeOOH nanosheets exposes abundant edge active sites. The heterogeneous interface between CeO_{2-x} and NiFeOOH leads to favorable electron transfer from $Ni^{2+/3+}$ and Fe^{3+} to $Ce^{3+/4+}$. The resulted high-valent Ni sites are more likely to enhance OH^- adsorption and promote the formation of *OOH, thereby enhancing the OER intrinsic activity. Meanwhile, the abundant oxygen vacancies in CeO_{2-x} for NiFeOOH@CeO_{2-x}/NF accelerate the electron transport. NiFeOOH@CeO_{2-x}/NF only requires overpotential of 229 and 287 mV to reach a current density of 50 and 500 mA·cm^{-2}, respectively, with superior stability at 1000 mA·cm^{-2} for 500 h. Furthermore, the water electrolyzer with PtNi/NF||NiFeOOH@CeO_{2-x}/NF couple requires only 1.42 V and 1.60 V to achieve current densities of 10 and 500 mA·cm^{-2} in 1.0 M KOH, respectively. This advancement highlights the potential application of hierarchical NiFeOOH@CeO_{2-x} nanosheets arrays in the field of electrochemical water electrolysis.

Electronic Supplementary Material: Supplementary material (characterization of the control samples, BET data, and additional electrochemical measurement data) is available in the online version of this article at https://doi.org/10.26599/NR.2025.94907213.

Acknowledgements

This work was financially supported by the National Natural Science Foundation of China (No. 51822106).

Data availability

All data needed to support the conclusions in the paper are presented in the manuscript and the ESM. Additional data related to this paper may be requested from the corresponding author upon request.

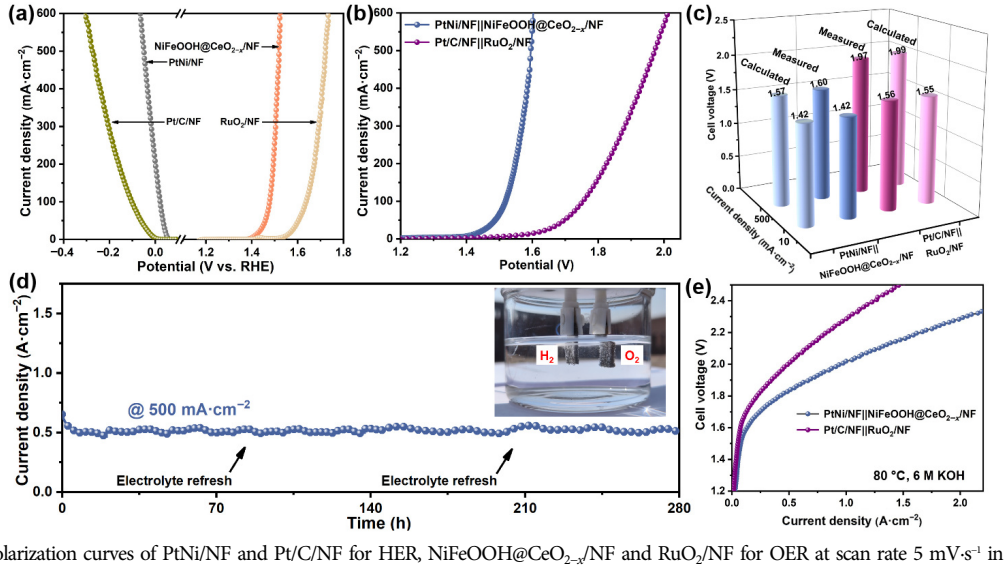

Figure 6 (a) LSV polarization curves of PtNi/NF and Pt/C/NF for HER, NiFeOOH@CeO_{2-x}/NF and RuO_2/NF for OER at scan rate 5 mV·s^{-1} in 1 M KOH. (b) LSV polarization curve of overall water splitting electrolyzer composed of PtNi/NF||NiFeOOH@CeO_{2-x}/NF and Pt/C/NF||RuO_2/NF in 1.0 M KOH. (c) Cell voltage of overall water splitting electrolyzer based on theoretical and measured values at different current densities. (d) Long-term durability of overall water splitting at a current density of 500 mA·cm^{-2}. Inset is an optical photograph of the water splitting electrolyzer. (e) Polarization curves of alkaline water electrolysis single cell under industrial conditions.

Declaration of competing interest

All the contributing authors report no conflict of interests in this work.

Author contribution statement

W. Z.: Data curation, formal analysis, investigation, software, writing – original draft. L. Y. X.: Formal analysis, writing – review & editing. X. R. H.: Formal analysis, data curation. C. Y. H.: Software, data curation. Y. L.: Formal analysis, investigation. J. T. Z.: Software, data curation. H. W. T.: Formal analysis, supervision. R. Z.: Conceptualization, supervision. P. F. Y.: Conceptualization, supervision. C. K. D.: Conceptualization, supervision. H. L.: Writing – review & editing. X. W. D.: Conceptualization, supervision, writing – review & editing. J. Y.: Conceptualization, funding acquisition, project administration, supervision, writing - review & editing.

Use of AI statement

None.

References

[1] Zhou, Y. N.; Li, F. T.; Dong, B.; Chai, Y. M. Double self-reinforced coordination modulation constructing stable Ni^{4+} for water oxidation. *Energy Environ. Sci.* **2024**, *17*, 1468–1481.

[2] Wei, A. M.; Deng, J. J.; Lu, C.; Wang, H.; Yang, B.; Zhong, J. $Fe_2(MoO_4)_3$ modified hematite with oxygen vacancies for high-efficient water oxidation. *Chem. Eng. J.* **2020**, *395*, 125127.

[3] Qian, G. F.; Chen, J. L.; Jiang, W. J.; Yu, T. Q.; Tan, K. X.; Yin, S. B. Strong electronic coupling of CoNi and N-doped-carbon for efficient urea-assisted H_2 production at a large current density. *Carbon Energy* **2023**, *5*, e368.

[4] Li, M.; Gu, Y.; Chang, Y. J.; Gu, X. C.; Tian, J. Q.; Wu, X.; Feng, L. G. Iron doped cobalt fluoride derived from CoFe layered double hydroxide for efficient oxygen evolution reaction. *Chem. Eng. J.* **2021**, *425*, 130686.

[5] Lu, C.; Zhang, D.; Wu, Z. Y.; Zhao, X. Q.; Feng, K.; Zhang, G. T.; Wang, S. A.; Kang, Z. H.; Zhong, J. Hetero phase modulated hematite photoanodes for practical solar water splitting. *Appl. Catal. B: Environ.* **2023**, *331*, 122695.

[6] Bai, L. C.; Lee, S.; Hu, X. L. Spectroscopic and electrokinetic evidence for a bifunctional mechanism of the oxygen evolution reaction. *Angew. Chem., Int. Ed.* **2021**, *60*, 3095–3103.

[7] Zhang, R. R.; Han, Y.; Wu, Q. L.; Lu, M.; Liu, G. S.; Guo, Z. T.; Zhang, Y. W.; Zeng, J. R.; Wu, X. F.; Zhang, D. D. et al. Electron accumulation induced by electron injection-incomplete discharge on NiFe LDH for enhanced oxygen evolution reaction. *Small* **2024**, *20*, 2402397.

[8] Dong, Y. W.; Liu, H. J.; Wang, X.; Wang, F. L.; Zhang, X. Y.; Lv, Q. X.; Liu, C. Y.; Chai, Y. M.; Dong, B. Manganese doping regulated the built-in electric field of FeBTC for enhanced photoelectrocatalytic hydrolysis. *Appl. Catal. B: Environ.* **2023**, *328*, 122464.

[9] Zang, Z. H.; Ren, Y. Y.; Fan, C. Y.; Cheng, Y. H.; Li, L. L.; Yu, X. F.; Yang, X. J.; Lu, Z. M.; Zhang, X. H.; Liu, H. Constructing unsaturated coordination Co–M (M = P, S, Se, Te) bonds modified metallic Co for efficient alkaline hydrogen evolution. *Appl. Catal. B: Environ.* **2024**, *350*, 123912.

[10] Li, M.; Wang, Y.; Zheng, Y.; Fu, G. T.; Sun, D. M.; Li, Y. F.; Tang, Y. W.; Ma, T. Y. Gadolinium-induced valence structure engineering for enhanced oxygen electrocatalysis. *Adv. Energy Mater.* **2020**, *10*, 1903833.

[11] Steimle, B. C.; Fenton, J. L.; Schaak, R. E. Rational construction of a scalable heterostructured nanorod megalibrary. *Science* **2020**, *367*, 418–424.

[12] Li, X. P.; Zheng, L. R.; Liu, S. J.; Ouyang, T.; Ye, S. Y.; Liu, Z. Q. Heterostructures of NiFe LDH hierarchically assembled on MoS_2 nanosheets as high-efficiency electrocatalysts for overall water splitting. *Chin. Chem. Lett.* **2022**, *33*, 4761–4765.

[13] Shao, Y.; Xiao, X.; Zhu, Y. P.; Ma, T. Y. Single-crystal cobalt phosphate nanosheets for biomimetic oxygen evolution in neutral electrolytes. *Angew. Chem., Int. Ed.* **2019**, *58*, 14599–14604.

[14] Bao, W. T.; Lu, K.; Fu, P. J.; Yang, J. F.; Tang, Y.; Sun, Y. X.; Yang, Z.; Bao, F. X.; Wang, Z. Y.; Yang, X. D. et al. Solution plasma-assisted synthesis of oxyhydroxides for advanced electrocatalytic water splitting. *Chem. Eng. J.* **2023**, *474*, 145826.

[15] Liu, J. C.; Qian, G. F.; Yu, T. Q.; Chen, J. L.; Zhu, C. W.; Li, Y.; He, J. J.; Luo, L.; Yin, S. B. Amorphous-crystalline heterostructure for simulated practical water splitting at high-current-density. *Chem. Eng. J.* **2022**, *431*, 134247.

[16] Hausmann, J. N.; Menezes, P. V.; Vijaykumar, G.; Laun, K.; Diemant, T.; Zebger, I.; Jacob, T.; Driess, M.; Menezes, P. W. In-liquid plasma modified nickel foam: NiOOH/NiFeOOH active site multiplication for electrocatalytic alcohol, aldehyde, and water oxidation. *Adv. Energy Mater.* **2022**, *12*, 2202098.

[17] Jia, C. X.; Zhen, C.; Yin, L. C.; Zhu, H. Z.; Du, P. P.; Han, A. L.; Liu, G.; Cheng, H. M. Topologic transition-induced abundant undercoordinated Fe active sites in NiFeOOH for superior oxygen evolution. *Nano Energy* **2023**, *106*, 108044.

[18] Jiao, H.; Wang, C.; Zhang, Z. Y.; Song, Y. F.; Feng, B. Q.; Na, P.; Wang, Z. L. Ultrafine NiFe-based (oxy)hydroxide nanosheet arrays with rich edge planes and superhydrophilic-superaerophobic characteristics for oxygen evolution reaction. *Small* **2023**, *19*, 2301609.

[19] Li, J. W.; Song, J. D.; Huang, B. Y.; Liang, G. F.; Liang, W. L.; Huang, G. J.; Jin, Y. Q.; Zhang, H.; Xie, F. Y.; Chen, J. et al. Enhancing the oxygen evolution reaction performance of NiFeOOH electrocatalyst for Zn-air battery by N-doping. *J. Catal.* **2020**, *389*, 375–381.

[20] van der Heijden, O.; Eggebeen, J. J. J.; Trzesniowski, H.; Deka, N.; Golnak, R.; Xiao, J.; van Rijn, M.; Mom, R. V.; Koper, M. T. M. Li^+ Cations activate NiFeOOH for oxygen evolution in sodium and potassium hydroxide. *Angew. Chem., Int. Ed.* **2024**, *63*, e202318692.

[21] Zhong, D. Z.; Zhang, L.; Li, C. C.; Li, D. D.; Wei, C. C.; Zhao, Q.; Li, J. P.; Gong, J. L. Nanostructured NiFe (oxy)hydroxide with easily oxidized Ni towards efficient oxygen evolution reactions. *J. Mater. Chem. A* **2018**, *6*, 16810–16817.

[22] Zhang, Z. H.; Wang, C. L.; Ma, X. L.; Liu, F.; Xiao, H.; Zhang, J.; Lin, Z.; Hao, Z. P. Engineering ultrafine NiFe-LDH into self-supporting nanosheets: Separation-and-reunion strategy to expose additional edge sites for oxygen evolution. *Small* **2021**, *17*, 2103785.

[23] Niu, S.; Jiang, W. J.; Tang, T.; Yuan, L. P.; Luo, H.; Hu, J. S. Autogenous growth of hierarchical $NiFe(OH)_x$/FeS nanosheet-on-microsheet arrays for synergistically enhanced high-output water oxidation. *Adv. Funct. Mater.* **2019**, *29*, 1902180.

[24] Wang, H. Y.; Hsu, Y. Y.; Chen, R.; Chan, T. S.; Chen, H. M.; Liu, B. Ni^{3+}-induced formation of active NiOOH on the spinel Ni–Co oxide surface for efficient oxygen evolution reaction. *Adv. Energy Mater.* **2015**, *5*, 1500091.

[25] Chen, W. Y.; Han, B.; Xie, Y. L.; Liang, S. J.; Deng, H.; Lin, Z. Ultrathin Co–Co LDHs nanosheets assembled vertically on MXene: 3D nanoarrays for boosted visible-light-driven CO_2 reduction. *Chem. Eng. J.* **2020**, *391*, 123519.

[26] Yao, N.; Wang, G. W.; Jia, H. N.; Yin, J. L.; Cong, H. J.; Chen, S. L.; Luo, W. Intermolecular energy gap-induced formation of high-valent cobalt species in CoOOH surface layer on cobalt sulfides for efficient water oxidation. *Angew. Chem., Int. Ed.* **2022**, *61*, e202117178.

[27] Shin, H.; Xiao, H.; Goddard, W. A. In silico discovery of new dopants for Fe-doped Ni oxyhydroxide ($Ni_{1-x}Fe_xOOH$) catalysts for oxygen evolution reaction. *J. Am. Chem. Soc.* **2018**, *140*, 6745–6748.

[28] Lee, D.; Gao, X.; Sun, L. X.; Jee, Y.; Poplawsky, J.; Farmer, T. O.; Fan, L. S.; Guo, E. J.; Lu, Q. Y.; Heller, W. T. et al. Colossal oxygen vacancy formation at a fluorite-bixbyite interface. *Nat. Commun.* **2020**, *11*, 1371.

[29] Obata, K.; Takanabe, K. A permselective CeO_x coating to improve the stability of oxygen evolution electrocatalysts. *Angew. Chem., Int. Ed.* **2018**, *57*, 1616–1620.

[30] Hu, Y. M.; Liu, W. J.; Jiang, K.; Xu, L.; Guan, M. L.; Bao, J.; Ji, H. B.; Li, H. M. Constructing a CeO_{2-x}@CoFe-layered double hydroxide heterostructure as an improved electrocatalyst for highly efficient water oxidation. *Inorg. Chem. Front.* **2020**, *7*, 4461–4468.

[31] Du, Y.; Liu, D. P.; Li, T. Z.; Yan, Y. D.; Liang, Y.; Yan, S. C.; Zou, Z. G. A phase transformation-free redox couple mediated electrocatalytic oxygen evolution reaction. *Appl. Catal. B: Environ.* **2022**, *306*, 121146.

[32] Jiao, H.; Wang, C.; Tian, H.; Zhang, Z. Y.; Zhao, Y.; Na, P.; Yamauchi, Y.; Wang, Z. L. Strong interaction heterointerface of NiFe oxyhydroxide/cerium oxide for efficient and stable water oxidation. *Chem. Eng. J.* **2024**, *498*, 155063.

[33] Dong, Q. B.; Shuai, C.; Mo, Z. L.; Liu, N. J.; Liu, G. G.; Wang, J.; Pei, H. B.; Jia, Q. Q.; Liu, W. T.; Guo, X. D. CeO_2 nanoparticles@NiFe-LDH nanosheet heterostructure as electrocatalysts for oxygen evolution reaction. *J. Solid State Chem.* **2021**, *296*, 121967.

[34] Bose, R.; Karuppasamy, K.; Rajan, H.; Velusamy, D. B.; Kim, H. S.; Alfantazi, A. Electrodeposition of unary oxide on a bimetallic hydroxide as a highly active and stable catalyst for water oxidation. *ACS Sustainable Chem. Eng.* **2019**, *7*, 16392–16400.

[35] Zhou, M.; Cheng, C. Q.; Dong, C. K.; Xiao, L. Y.; Zhao, Y.; Liu, Z. W.; Zhao, X. R.; Sasaki, K.; Cheng, H.; Du, X. W. et al. Dislocation network-boosted PtNi nanocatalysts welded on nickel foam for efficient and durable hydrogen evolution at ultrahigh current densities. *Adv. Energy Mater.* **2023**, *13*, 2202595.

[36] Lin, Z.; Bu, P. P.; Xiao, Y.; Gao, Q. L.; Diao, P. β- and γ-NiFeOOH electrocatalysts for an efficient oxygen evolution reaction: An electrochemical activation energy aspect. *J. Mater. Chem. A* **2022**, *10*, 20847–20855.

[37] Wu, L. B.; Ning, M. H.; Xing, X. X.; Wang, Y.; Zhang, F. H.; Gao, G. H.; Song, S. W.; Wang, D. Z.; Yuan, C. Q.; Yu, L. et al. Boosting oxygen evolution reaction of (Fe,Ni)OOH via defect engineering for anion exchange membrane water electrolysis under industrial conditions. *Adv. Mater.* **2023**, *35*, 2306097.

[38] Xiao, L. Y.; Yang, T. T.; Cheng, C. Q.; Du, X. W.; Zhao, Y.; Liu, Z. W.; Zhao, X. R.; Zhang, J. T.; Zhou, M.; Han, C. Y. et al. Coupled compressive-tensile stains boosting both activity and durability of NiMo electrode for alkaline water/seawater hydrogen evolution at high current densities. *Chem. Eng. J.* **2024**, *485*, 150044.

[39] Liu, Y.; Xiao, L. Y.; Tan, H. W.; Zhang, J. T.; Dong, C. K.; Liu, H.; Du, X. W.; Yang, J. Amorphous/crystalline phases mixed nanosheets array rich in oxygen vacancies boost oxygen evolution reaction of spinel oxides in alkaline media. *Small* **2024**, *20*, 2401504.

[40] Zhang, Y. C.; Li, Z.; Zhang, L.; Pan, L.; Zhang, X. W.; Wang, L.; Fazal-E-Aleem, N.; Zou, J. J. Role of oxygen vacancies in photocatalytic water oxidation on ceria oxide: Experiment and DFT studies. *Appl. Catal. B: Environ.* **2018**, *224*, 101–108.

[41] Wang, Z. Q.; Lei, Q. J.; Wang, Z. Y.; Yuan, H. M.; Cao, L. J.; Qin, N.; Lu, Z. G.; Xiao, J. X.; Liu, J. L. *In-situ* synthesis of free-standing FeNi-oxyhydroxide nanosheets as a highly efficient electrocatalyst for water oxidation. *Chem. Eng. J.* **2020**, *395*, 125180.

[42] Wang, K.; Du, H. F.; He, S.; Liu, L.; Yang, K.; Sun, J. M.; Liu, Y. H.; Du, Z. Z.; Xie, L. H.; Ai, W. et al. Kinetically controlled, scalable synthesis of γ-FeOOH nanosheet arrays on nickel foam toward efficient oxygen evolution: The key role of *in-situ*-generated γ-NiOOH. *Adv. Mater.* **2021**, *33*, 2005587.

[43] Luo, Q. M.; Zhao, Y. W.; Sun, L.; Wang, C.; Xin, H. Q.; Song, J. X.; Li, D. Y.; Ma, F. Interface oxygen vacancy enhanced alkaline hydrogen evolution activity of cobalt-iron phosphide/CeO_2 hollow nanorods. *Chem. Eng. J.* **2022**, *437*, 135376.

[44] Wen, S. T.; Huang, J.; Li, T. T.; Chen, W.; Chen, G. L.; Zhang, Q.; Zhang, X. H.; Qian, Q. Y.; Ostrikov, K. Multiphase nanosheet-nanowire cerium oxide and nickel-cobalt phosphide for highly-efficient electrocatalytic overall water splitting. *Appl. Catal. B: Environ.* **2022**, *316*, 121678.

[45] Xia, J. L.; Zhao, H. Y.; Huang, B. L.; Xu, L. L.; Luo, M.; Wang, J. W.; Luo, F.; Du, Y. P.; Yan, C. H. Efficient optimization of electron/oxygen pathway by constructing ceria/hydroxide interface for highly active oxygen evolution reaction. *Adv. Funct. Mater.* **2020**, *30*, 1908367.

[46] Zhang, J.; He, W. H.; Aiyappa, H. B.; Quast, T.; Dieckhöfer, S.; Öhl, D.; Junqueira, J. R. C.; Chen, Y. T.; Masa, J.; Schuhmann, W. Hollow CeO_2@Co_2N nanosheets derived from Co-ZIF-L for boosting the oxygen evolution reaction. *Adv. Mater. Interfaces* **2021**, *8*, 2100041.

[47] Li, W. M.; Zhao, L. S.; Wang, C.; Lu, X. F.; Chen, W. Interface engineering of heterogeneous CeO_2–CoO nanofibers with rich oxygen vacancies for enhanced electrocatalytic oxygen evolution performance. *ACS Appl. Mater. Interfaces* **2021**, *13*, 46998–47009.

[48] Lu, Z.; Wang, J. K.; Zhang, P. F.; Guo, W. H.; Shen, Y. Q.; Liu, P. Z.; Ji, J. L.; Du, H. Y.; Zhao, M.; Liang, H. J. et al. Directed electron transport induced surface reconstruction of 2D NiFe-LDH/stanene heterojunction catalysts for efficient oxygen evolution. *Appl. Catal. B: Environ.* **2024**, *353*, 124073.

[49] Liu, Y.; Liu, X. H.; Jadhav, A. R.; Yang, T.; Hwang, Y.; Wang, H. D.; Wang, L. L.; Luo, Y. G.; Kumar, A.; Lee, J. et al. Unraveling the function of metal-amorphous support interactions in single-atom electrocatalytic hydrogen evolution. *Angew. Chem., Int. Ed.* **2022**, *61*, e202114160.

[50] Habibi, E.; Razmi, H. Glycerol electrooxidation on Pd, Pt and Au nanoparticles supported on carbon ceramic electrode in alkaline media. *Int. J. Hydrogen Energy* **2012**, *37*, 16800–16809.

[51] Geng, S. K.; Zheng, Y.; Li, S. Q.; Su, H.; Zhao, X.; Hu, J.; Shu, H. B.; Jaroniec, M.; Chen, P.; Liu, Q. H. et al. Nickel ferrocyanide as a high-performance urea oxidation electrocatalyst. *Nat. Energy* **2021**, *6*, 904–912.

[52] He, Z. Y.; Zhang, J.; Gong, Z. H.; Lei, H.; Zhou, D.; Zhang, N.; Mai, W.; Zhao, S. J.; Chen, Y. Activating lattice oxygen in NiFe-based (oxy)hydroxide for water electrolysis. *Nat. Commun.* **2022**, *13*, 2191.

[53] Chen, Z. L.; Yang, H. Y.; Mebs, S.; Dau, H.; Driess, M.; Wang, Z. W.; Kang, Z. H.; Menezes, P. W. Reviving oxygen evolution electrocatalysis of bulk La–Ni intermetallics via gaseous hydrogen engineering. *Adv. Mater.* **2023**, *35*, 2208337.

[54] Qiu, Z.; Tai, C. W.; Niklasson, G. A.; Edvinsson, T. Direct observation of active catalyst surface phases and the effect of dynamic self-optimization in NiFe-layered double hydroxides for alkaline water splitting. *Energy Environ. Sci.* **2019**, *12*, 572–581.

[55] Mondal, I.; Hausmann, J. N.; Vijaykumar, G.; Mebs, S.; Dau, H.; Driess, M.; Menezes, P. W. Nanostructured intermetallic nickel silicide (pre)catalyst for anodic oxygen evolution reaction and selective dehydrogenation of primary amines. *Adv. Energy Mater.* **2022**, *12*, 2200269.

[56] Xu, J. C.; Wang, B. X.; Lyu, D. Y.; Wang, T. W.; Wang, Z. Y. *In situ* Raman investigation of the femtosecond laser irradiated NiFeOOH for enhanced electrochemical ethanol oxidation reaction. *Int. J. Hydrogen Energy* **2023**, *48*, 10724–10736.